INTERNATIONAL JOURNAL FOR NUMERICAL METHODS IN FLUIDS, VOL. 16, 777–791 (1993)

TREATMENT OF VORTEX SHEETS FOR THE TRANSONIC FULL-POTENTIAL EQUATION

T. Q. DANG

Department of Mechanical, Aerospace and Manufacturing Engineering, Syracuse University, Syracuse, NY 13244, U.S.A.

SUMMARY

This paper summarizes a combined analytical–computational technique which models vortex sheets in transonic potential-flow methods. In this approach, the inviscid nature of discontinuities across vortex sheets is preserved by employing the step function to remove singularities at these surfaces. The location and strength of the vortex sheets are determined by satisfying the flow-tangency boundary condition and the vorticity transport equation. The theory is formulated for the general three-dimensional case, but its application is confined to the problem of computing slipstreams behind propellers with free-vortex blading in axisymmetric flows.

KEY WORDS Vortex sheet Propeller slipstream Propeller–airframe integration Finite volume Full potential Transonic flow

1. INTRODUCTION

Transonic-flow computational methods based on the full-potential equation have played an important role in the past decade in the design of fuel-efficient aircrafts. In particular, the finite-volume algorithm of Jameson and Caughey,[1,2] a generalization of the type-dependent differencing concept of Murman and Cole,[3] has been widely used. In addition, progress in three-dimensional grid generation methods[4] along with the development of the multigrid technique[5,6] has greatly improved the usefulness of the full-potential approach. Consequently, a large number of transonic potential-flow codes are routinely used in industry.

The irrotational-flow assumption prevents the full-potential approach from predicting accurately the flows in which the effect of the vorticity field is important. For example, the calculations of shock location and shock strength by the full-potential method deteriorate as the shock Mach number increases because of the neglection of the vorticity field generated behind these shocks. In this case, several authors[7–9] have improved shock calculations through the use of Euler correction methods. These authors have shown that the Euler correction methods yield shock calculations similar to those using Euler methods[10,11] for both two- and three-dimensional flows in the presence of strong shocks. In addition, the Euler correction method has been employed to model the rotational flowfield behind propellers with forced-vortex blading.[12]

Another weakness of the full-potential approach is its inability to model accurately vortex sheets such as the trailing-vortex sheet shed behind a finite wing or the slipstream behind a propeller with free-vortex blading. As the full-potential method does not satisfy the dynamic condition on these vortex sheets (i.e. the vorticity transport equation), it is necessary to use simplified models to describe these vortex sheets. In the case of the trailing-vortex sheet, its

0271–2091/93/090777–15$12.50

Received 8 May 1990
Revised 13 July 1992

location is usually taken to be the grid surface emanating from the wing trailing edge, and the vortex strength is modelled using the linearized wing theory.[2] In the case of the propeller slipstream, its location is taken to be the grid surface emanating from the propeller tip, and the equal-pressure condition across the propeller slipstream is approximately satisfied by enforcing the jump in the magnitude of the velocity along an assumed direction.[13]

With the recent interest in the fuel-efficient aft-fuselage-mounted propfan airplane, accurate calculations of these vortex sheets become critical. For example, the designer is concerned with the location of the propeller installation so as to make sure that the wing wake does not intersect the propeller disk. In this case, the method proposed by Steinhoff and Ramachandran[14] can be used to handle this problem. Also, studies[12,13] indicate that accurate propeller–airframe interference calculations require an accurately defined propeller slipstream geometry.

This paper presents an approach to model vortex sheets using the existing full-potential methods. The idea is to remove singularities in the flowfield at the vortex sheets using generalized functions:[15] all discontinuities are expressed in terms of the step function. The location and strength of the vortex sheets are determined by satisfying the flow-tangency boundary condition and the vorticity transport equation, respectively. The technique presented in this paper can be considered to be the external-flow version of the 'smoothing' expansion technique[16–18] developed earlier for periodic internal flows. Although the purpose of this paper is to introduce a technique of capturing various types of vortex sheets for full-potential methods, a simple example of its actual use is presented to facilitate the task of describing the technique. The example chosen is the capturing of propeller slipstream surfaces which arise from the presence of nacelle-mounted counter-rotating propellers with free-vortex blading.

2. POTENTIAL–MULTIENERGY FLOW ACTUATOR DISK MODEL

Recent advances in turboprop or Ultra High Bypass (UHB) engine development have stimulated great interests in advanced propfan airplane design. The concern of an airplane designer is not focused on the details of the blade-to-blade flowfield, but rather on the interference effects of the propfan on the airframe. In this case the simple actuator disk model appears to be more than adequate.[12,13,19,20] Furthermore, recent work[12,13] has indicated that the detailed structure of the rotational flowfield within and behind the propeller, namely, the propeller bound and trailing vorticities, does not play an important role in propeller–airframe interference studies. Hence, an actuator disk with free-vortex blading can be used to simulate propeller effects effectively; the prescribed jump in the stagnation enthalpy across the actuator disk, denoted by Δh_0, is assumed to be constant (Figure 1). In addition, the counter-rotating propeller is assumed to be ideal so that the flow is isentropic across the propeller and the jump in the circumferential velocity (or swirl) across the propeller is zero.

Using the above model, the flowfield consists of two potential-flow regions, each having different prescribed stagnation conditions, separated by a bound-vortex sheet at the actuator disk and a free-vortex sheet on the propeller slipstream (Figure 1). This model is called the potential–multienergy flow actuator disk model in this study. In this example, the location and strength of the bound-vortex sheet is prescribed, while those of the free-vortex sheet are not known *a priori* and must be determined during the calculation. Across this free-vortex sheet, two conditions must be satisfied:

1. *The flow-tangency boundary condition.* This is a kinematic condition which is satisfied by ensuring that the vortex sheet coincides with the stream surface emanating from the tip of the propeller.

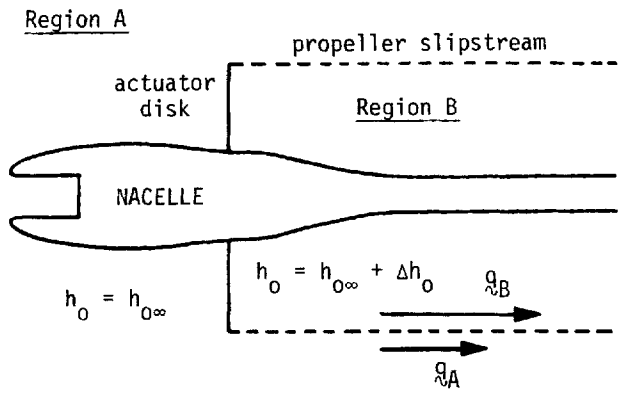

Figure 1. Potential–multienergy flow actuator disk model for a counter-rotating propeller

2. *The equal-pressure condition.* This is a dynamic condition which can be satisfied by invoking the vorticity transport equation. As the two potential-flow regions have different stagnation conditions, this condition implies that the velocity vector is discontinuous in magnitude and possibly in direction (i.e. for three-dimensional flows) across this vortex sheet (Figure 1).

For the purpose of completeness, it is interesting to note that in practice, it is more useful to prescribe the propeller thrust loading coefficient rather than the jump in the stagnation enthalpy across the actuator disk. Using the one-dimensional, incompressible-flow Froude–Rankine analysis, the jump in the stagnation enthalpy across the actuator disk is related to the thrust loading coefficient by

$$\Delta h_0 = \frac{1}{2}\left(\frac{T}{QA_d}\right), \tag{1}$$

where T is the thrust, Q is the dynamic pressure, and A_d is the propeller frontal area. Equation (1) is used as the initial guess for the required stagnation enthalpy jump corresponding to the prescribed thrust loading coefficient. The actual thrust loading coefficient is computed from the momentum integral equation using the converged solution. Numerical experiments have shown that this relationship is accurate throughout the practical range of the thrust loading coefficient.

3. PRIMITIVE APPROACH

A conceptually easy-to-understand procedure to handle the discontinuity at the free-vortex sheet is to use a full-potential approach with boundary conforming grid at the propeller slipstream.[13,21] In this method, the grid line leaving the actuator disk tip is either assumed to be the slipstream, or modified during the calculation to conform to the actual slipstream. The equal-pressure condition, which requires

$$q_B^2 - q_A^2 = 2\Delta h_0 \tag{2}$$

is satisfied by enforcing a double-valued potential along this grid line. Here q_A and q_B are the total velocities on the propeller slipstream in region A and region B, respectively (Figure 1).

Although this rather simple approach appears to be attractive, it has several restrictions and disadvantages:

1. The enforcement of the equal-pressure condition through equation (2) is not complete because it does not say anything about the direction of the velocity jump. In the axisymmetric case, this condition can be satisfied exactly since the directions of the velocities q_A and q_B are known. However, in the general three-dimensional case, the velocity jump is known to lie on the propeller slipstream surface, but its direction must be extracted from the vorticity transport equation. In practice, the jump in the velocity is assumed to be along the streamwise grid lines.
2. The required use of the adaptive grid technique to satisfy the propeller slipstream kinematic condition is not desirable because it tends to slow down convergence and can introduce instabilities into the calculation.

4. PRESENT APPROACH

The results and findings of the investigation described in Section 3 suggest the usefulness of a technique which does not require the fitting of a grid surface to the propeller slipstream during the calculation. In addition, accurate modelling of this vortex sheet requires the satisfaction of the vorticity transport equation which describes the convection of the vortex filaments lying on this surface. The 'smoothing' technique described in this section is such a technique.

4.1. Smoothing technique

The smoothing technique[16] consists of removing the singular part of the flowfield at the vortex sheet through properly chosen generalized functions. Consider the velocity profile at an axial location which crosses a vortex sheet, its location being at $\lambda=0$ (Figure 2). In this case, the velocity is decomposed into two parts:

$$u(\lambda)=u_0(\lambda)+H(\lambda)\Delta u. \tag{3}$$

In equation (3), the step function denoted by $H(\lambda)$ is used to represent the velocity jump Δu across the propeller slipstream. As a result, the remaining part of the flowfield denoted by $u_0(\lambda)$ is smooth. Here the step function $H(\lambda)$ is defined as

$$H(\lambda)=\begin{cases}1, & \lambda>0,\\ 0, & \lambda<0.\end{cases} \tag{4}$$

Recall that the gradient of the step function is related to the Dirac delta function[15]

$$\nabla H=\delta(\lambda)\nabla\lambda, \tag{5}$$

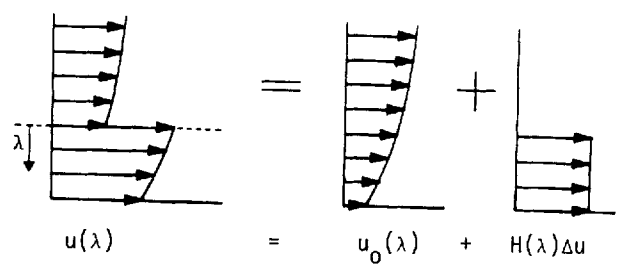

Figure 2. 'Smoothing' technique applied to velocity

where the Dirac delta function $\delta(\lambda)$ is defined as zero everywhere except at $\lambda=0$ and

$$\int_{-\infty}^{\infty} \delta(\lambda)\,\mathrm{d}\lambda = 1{\cdot}0. \tag{6}$$

4.2. Theory

In this section, the smoothing technique is applied to the problem of simulating propeller effects using the potential–multienergy flow actuator disk model (see Section 2). In general, as the velocity vector is allowed to have a jump not only across the propeller slipstream, but also across the actuator disk, it can be expressed as

$$\mathbf{V} = \nabla\phi + H(z^*)H(\zeta)\Delta h_0 \nabla t, \tag{7}$$

where $z^* \equiv z - z_{\text{disk}} = 0$ defines the actuator disk plane, and $\zeta \equiv f(z) - r = 0$ defines the propeller slipstream surface (Figure 3).

Taking the curve of equation (7), the vorticity vector takes the form

$$\boldsymbol{\Omega} = \delta(z^*)\{H(\zeta)\Delta h_0[\hat{e}_z \times \nabla t]\} + \delta(\zeta)\{H(z^*)\Delta h_0[\nabla\zeta \times \nabla t]\}. \tag{8}$$

As required, the vorticity vector is zero everywhere except at the actuator disk [first term on the right-hand side of equation (8)] and at the propeller slipstream [last term on the right-hand side of equation (8)]. In equation (7), the Clebsch[22] representation of the velocity vector is employed. This type of decomposition of the velocity vector into potential and rotational parts has been extensively employed in the calculations of three-dimensional rotational flows in turbomachines up to the subcritical flow regime using mostly analytical approaches.[22–27] Recently, an Euler correction method was developed based on the Clebsch transformation to model shear flows in full-potential methods such as the vorticity field generated behind shocks[9] and the rotational flowfield behind propellers with forced-vortex blading.[12] Similar use of the Clebsch transformation has been proposed by Steinhoff and Ramachandran[14] to handle the wakes in helicopter rotor flowfields.

To determine the flowfield, these Clebsch variables are chosen to satisfy the equations of motion. For steady flow, the continuity equation is

$$\nabla \cdot (\rho \mathbf{V}) = 0, \tag{9}$$

while the momentum equation written in Crocco's form for isentropic flow is

$$\mathbf{V} \times \boldsymbol{\Omega} = \nabla h_0 + \mathbf{F}, \tag{10}$$

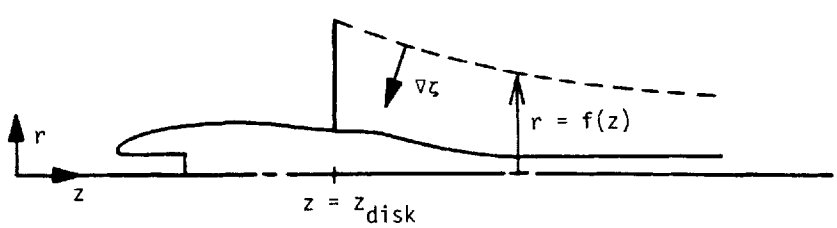

Figure 3. Geometrical definitions

where **F** is a body force per unit mass. This body force term is similar to the prescribed finite-volume force vector employed by Whitfield and Jameson[19] in their calculation of propeller–airframe interaction. In the present model (Figure 1), given the locations of the actuator disk and the propeller slipstream, the stagnation enthalpy field can be expressed as

$$h_0 = h_{0\infty} + H(z^*)H(\zeta)\Delta h_0. \tag{11}$$

Furthermore, the body force **F** is concentrated at the actuator disk and can be expressed as

$$\mathbf{F} = \delta(z^*)H(\zeta)[F_r\hat{e}_r + F_z\hat{e}_z] \tag{12}$$

In the present approach, the potential part ϕ in equation (7) is determined using the continuity equation, while the Clebsch variable t is chosen to satisfy the momentum equation. On substituting equations (8), (11) and (12) into equation (10), along with the use of vector identities, the following are obtained. Along the actuator disk, the momentum equation reduces to

$$\Delta h_0\{(\langle \mathbf{V}\rangle_d \cdot \nabla t)\hat{e}_z - (\langle \mathbf{V}\rangle_d \cdot \hat{e}_z)\nabla t\} = F_r\hat{e}_r + F_z\hat{e}_z + \Delta h_0\hat{e}_z, \tag{13}$$

where $\langle\ \rangle_d$ denotes the average value in front and behind the actuator disk. Equating terms in the same direction, the body force per unit mass can be computed from

$$F_r = -\Delta h_0 \langle V_z\rangle_d \frac{\partial t}{\partial r}, \tag{14}$$

$$F_z = -\Delta h_0\left(1 - \langle V_r\rangle_d \frac{\partial t}{\partial r}\right). \tag{15}$$

Similarly, along the propeller slipstream behind the actuator disk, the momentum equation reduces to

$$(\langle \mathbf{V}\rangle_s \cdot \nabla t)\nabla\zeta - (\langle \mathbf{V}\rangle_s \cdot \nabla\zeta)\nabla t = \nabla\zeta, \tag{16}$$

where $\langle\ \rangle_s$ denotes the average value above and below the propeller slipstream. On imposing the flow-tangency boundary condition on the propeller slipstream, namely,

$$\langle \mathbf{V}\rangle_s \cdot \nabla\zeta = 0, \tag{17}$$

the governing equation for the Clebsch variable t is obtained:

$$\langle \mathbf{V}\rangle_s \cdot \nabla t = 1. \tag{18}$$

Conceptually, the Clebsch variable t is the classical Darwin–Lighthill–Hawthorne drift function.[22,28] In the general three-dimensional case, the variation of t from streamline to streamline lying on the propeller slipstream surface is directly connected to the stretching and tipping of the vortex filaments located on this surface. In fact, the drift function not only enforces the equal-pressure condition across the propeller slipstream, but also specifies the direction of the jump in the velocity, namely,

$$\mathbf{q}_B - \mathbf{q}_A = \Delta h_0 \nabla t. \tag{19}$$

Note that equation (19) combined with equation (18) is the generalization of equation (2). In principle, the flowfield can be computed by solving iteratively between the governing equation for the potential part [equation (9)] and the governing equations for the rotational part [equations (17) and (18)] subject to appropriate boundary conditions. The following subsections describe methods of solving these equations, along with the iterative procedure employed to determine the flowfield.

4.3. Solution method for the potential function

As mentioned in Section 4.1, the potential part ϕ in the expression for the velocity vector is chosen to satisfy the continuity equation. In the present study, the finite-volume full-potential method of Jameson and Caughey[1] is employed to determine the potential part. In this numerical scheme, the discretized quasi-linear form of the potential equation utilized for formulating the relaxation scheme is

$$L^n\{\phi_{i,j}^{n+1}-\phi_{i,j}^n\}=-\mathrm{RES}_{i,j}^n, \tag{20}$$

where n is the iterative level. In equation (20), the operator L on the correction is derived from the potential equation, and RES is the residual of the continuity equation.

When the present power method is included, the general form of the operator L remains unchanged. The only modifications involved are in the evaluations of the cell-averaged velocity, speed of sound and density which appear in the expression for the residual RES and in the coefficients of the operator L.

As an illustration for the method of computing cell-averaged quantities, consider the velocity vector. According to equation (7), the velocity vector takes on appropriate forms, depending upon the location of the cell under consideration (Figure 4). In the present study, the grid is constructed to conform to the specified actuator disk location and size but not to the propeller slipstream location since it is not known *a priori*. Hence, in general, there exist cells which lie in both regions A and B, such as cell AB shown in Figure 4. In this case, the method of area-weighted average is used to evaluate the cell-averaged quantities. For cell A, which lies in region A, the cell-averaged velocity is computed from

$$\mathbf{V}=\nabla\phi. \tag{21}$$

For cell B, which lies in region B, the cell-averaged velocity is computed from

$$\mathbf{V}=\nabla\phi+\Delta h_0\nabla t \tag{22}$$

and, finally, for cell AB, which lies in both regions, the cell-averaged velocity is computed from

$$\mathbf{V}=\frac{A_\mathrm{A}}{A_\mathrm{A}+A_\mathrm{B}}\nabla\phi+\frac{A_\mathrm{B}}{A_\mathrm{A}+A_\mathrm{B}}(\nabla\phi+\Delta h_0\nabla t), \tag{23}$$

where A_A is the cell area which lies in region A, and A_B is the cell area which lies in region B (Figure 4). This type of area-weighting is similar to the 'cloud in cell' of Baker.[29]

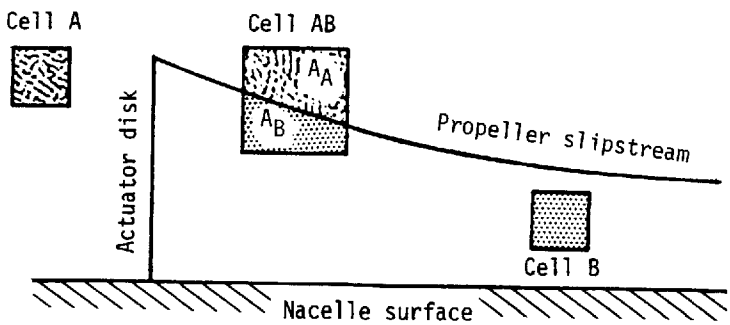

Figure 4. Method of area-weighted average applied to cell-averaged quantities

4.4. Solution method for the drift function

In the present formulation, the drift function t is employed to describe the convection of the vortex rings lying on the propeller slipstream. Hence, it is necessary to compute the drift function on the slipstream surface only. The distribution of the drift function t inside the propeller slipstream can be taken arbitrarily since, according to equation (7), it merely redefines the potential function there. The governing equation for t [equation (18)] can be simplified by invoking the propeller slipstream kinematic condition. Along the propeller slipstream, in addition to equation (17), the flow-tangency boundary condition also requires the jump in the velocity across this surface to be tangent to it. On using equation (19), this condition translates to

$$\nabla t \cdot \nabla \zeta = 0. \tag{24}$$

Equation (24) imposes a constraint on the derivatives of t and, along with the definition of ζ from Section 4.2, can be used to reduce equation (18) to

$$\left.\frac{\partial t}{\partial z}\right|_{\zeta=0} = \frac{1}{\langle V_z \rangle_s + \langle V_r \rangle_s (\mathrm{d}f/\mathrm{d}z)}. \tag{25}$$

Since the drift function itself is not used in the present formulation, but rather its gradient, the Clebsch variable t is updated during the calculation simply through algebraic relationships, namely, equations (24) and (25). In the general three-dimensional case,[30] a two-dimensional hyperbolic equation must be solved to determine the drift function.

4.5. Solution method for the propeller slipstream location

Using the definition of ζ defined in Section 4.2, the propeller slipstream kinematic condition [equation (17)] reduces to

$$\langle V_z \rangle_s \frac{\mathrm{d}f}{\mathrm{d}z} = \langle V_r \rangle_s. \tag{26}$$

Given the velocity field from the previous iteration step, the propeller slipstream location is determined by integrating numerically equation (26) from the actuator disk to the downstream region. The initial location of the propeller slipstream is at the tip of the actuator disk.

Two types of power simulation modes have been developed to investigate the importance of the propeller slipstream geometry. In the assumed propeller slipstream mode, the propeller slipstream is taken to be the grid line emanating from the tip of the actuator disk and is kept fixed during the calculation. In the computed slipstream mode, the initial guess of the propeller slipstream is chosen to be this grid line, but the propeller slipstream geometry is continuously updated during the calculation through equation (26). The outcome of this investigation will be discussed in Section 5.

4.6. Iterative procedure

The flowfield is determined by solving iteratively between the potential and the rotational parts defined in equation (7). The following iterative procedure is employed:

1. Set the initial velocity field to the freestream condition.
2. Update the potential function ϕ by advancing one multigrid cycle using a modified version of a finite-volume full-potential method described in Section 4.3. In this step, the implementation of the area weighted–averaged procedure to compute cell-averaged quantities

results in an increase of 25% in the computing time per iterative cycle over the original full-potential method.

3. Update the drift function t through algebraic relationships [equations (24) and (25)]. The computing time required in this step is negligible compared to the second step since the calculation is performed only on the propeller slipstream behind the actuator disk.
4. If the assumed slipstream mode is employed, bypass this step. Otherwise, in the computed slipstream mode, the propeller slipstream ζ is updated through equation (26). Again, the computing time required in this step is negligible compared to the second step.
5. Repeat steps 2–5 until convergence is attained.

Numerical experiments show that the increase in the computing time per multigrid cycle is roughly 30% relative to the original code. These calculations also show that in the practical range of the thrust loading coefficient, the number of cycles required to obtain a converged solution comparable to the prop-off case is only slightly increased, indicating that the present scheme is efficient. Finally, this proposed iterative procedure is stable throughout the practical range of the thrust loading coefficient.

5. RESULTS

The proposed method of handling vortex sheets has been implemented into an axisymmetric full-potential code[31] to simulate power effects for isolated nacelles at zero degree angle of attack. Generation of the computational grid is accomplished using the hybrid conformal-mapping–algebraic technique of Halsey.[32] This method conforms grid lines to a specified actuator disk location and size, along with the option of conforming the grid lines to an estimated location of the propeller slipstream.

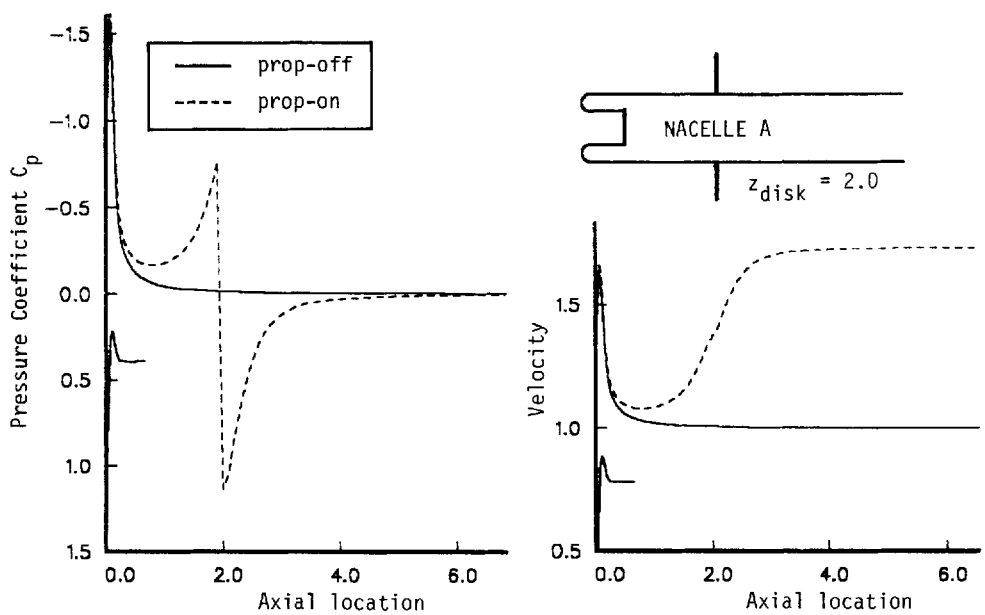

Figure 5. Comparison of surface pressure and total velocity distributions for nacelle A at $M_{\infty}=0{\cdot}2$ and $T/QA_d=2{\cdot}0$

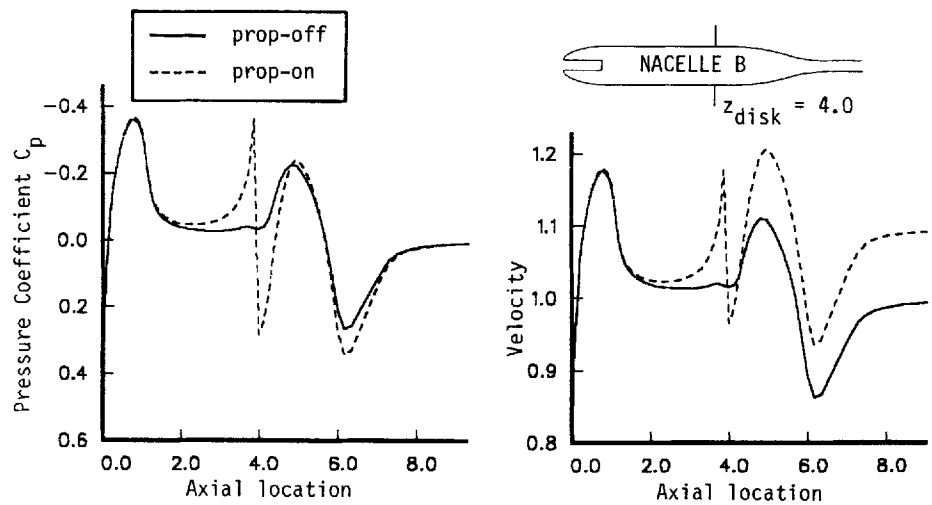

Figure 6. Comparison of surface pressure and total velocity distributions for nacelle B at $M_\infty = 0{\cdot}8$ and $T/QA_d = 0{\cdot}2$

Figure 5 shows comparisons of the surface pressure and total velocity distributions for the nacelle A between the prop-off and the prop-on cases at the subsonic flow regime ($M_\infty = 0{\cdot}2$, $T/QA_d = 2{\cdot}0$). As expected, the effects of power are to accelerate the flow in front of the propeller and to produce an increase in the static pressure across the propeller. In the absence of swirl, the computed farfield static pressure approaches the freestream condition. For incompressible flow, as is nearly the case here, the velocity is continuous across the actuator disk as required by the continuity equation. As the stagnation condition in region B is greater than that in region A, the farfield velocity within the propeller slipstream is greater than the freestream velocity, typically a two-to-one ratio in the practical subsonic regime. Figure 6 shows the same comparisons for the nacelle B at the transonic cruising condition ($M_\infty = 0{\cdot}8$, $T/QA_d = 0{\cdot}2$). Here the overall trend is the same as in Figure 5, except that compressibility effects do allow for a jump in the velocity across the actuator disk. Also, at the transonic cruising condition, the farfield slipstream-to-freestream velocity ratio is small, typically of the order of 1·1 for these advanced propellers. Consequently, the problem of capturing propeller slipstream surface is more difficult in the subsonic-flow regime than in the transonic-flow regime: propeller slipstream contraction is higher, and discontinuity in the velocity vector across the propeller slipstream is larger.

Plate 1 illustrates contour plots of pressure coefficient increments ΔC_p at the practical subsonic ($M_\infty = 0{\cdot}2$, $T/QA_d = 2{\cdot}0$) and transonic ($M_\infty = 0{\cdot}8$, $T/QA_d = 0{\cdot}2$) flow regimes around nacelle C. Here the pressure coefficient increment is defined to be the difference in the pressure coefficient between the prop-on and prop-off solutions. The actuator disk is located at the axial station where a sharp jump in ΔC_p exists. This figure, along with line plots of ΔC_p as a function of radial location at selected axial stations behind the actuator disk,[33] show that the pressure field is continuous across the propeller slipstream. This figure also indicates that propeller effects are much more pronounced in the practical subsonic flow regime than in the transonic flow regime. Plate 2 illustrates similar contour plots for the velocity increment ΔV. This figure shows a sharp jump in ΔV across the propeller slipstream behind the actuator disk. A closer look at the line plots of ΔV as a function of radial location at selected axial stations behind the actuator disk[33] show that the discontinuity in the velocity across the propeller slipstream is captured within one mesh point with no oscillation.

To investigate the sensitivity of the solutions to the grid distributions, calculations were carried out using the grids shown in Figure 7. Compared to the standard grid used in the earlier calculations, the distributions of the grid lines in grid A are forced to conform to the propeller slipstream as seen by the contraction of the grid lines behind the actuator disk. Grid A contains 96×24 cells. On the other hand, the grid lines in grid B are purposely chosen to deviate from the propeller slipstream shape, as seen by the divergence of the grid lines behind the actuator disk. In addition, the number of cells in the axial direction in grid B is reduced by half, i.e. to 48×24 cells. Figure 8 shows the grid lines emanating from the tip of the actuator disk taken from grids A and B. These grid lines are used either as the actual or the initial guesses for the propeller slipstream location in the following calculations.

Figure 9 illustrates comparisons of the nacelle surface pressure distributions between the prop-off and the prop-on cases which are computed using the grid A and grid B distributions. To demonstrate the importance of defining accurately the slipstream geometry, the plot on the left of Figure 9 shows the comparison with the prop-on solutions running in the assumed slipstream mode: the initial propeller slipstream shapes, shown in Figure 8, are kept fixed during the calculation. This figure shows that the predicted prop-on solutions are highly dependent on the propeller slipstream shape. On the other hand, when the computed slipstream mode is employed, namely, the propeller slipstream shape is continuously updated during the calculation, the predicted prop-on solutions are virtually identical. In fact, the computed farfield propeller slipstream radius taken from the converged solutions using grids A and B are $r/R_{\text{disk}} = 0{\cdot}9175$ and 0·9087, respectively.

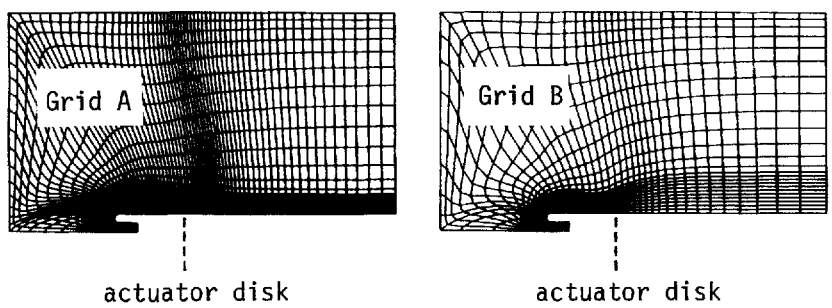

Figure 7. Illustration of grid A and grid B

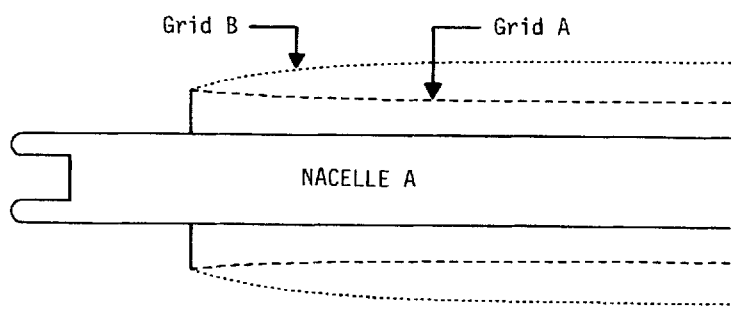

Figure 8. Illustration of grid lines emanating from tip of actuator disk taken from grid A and grid B

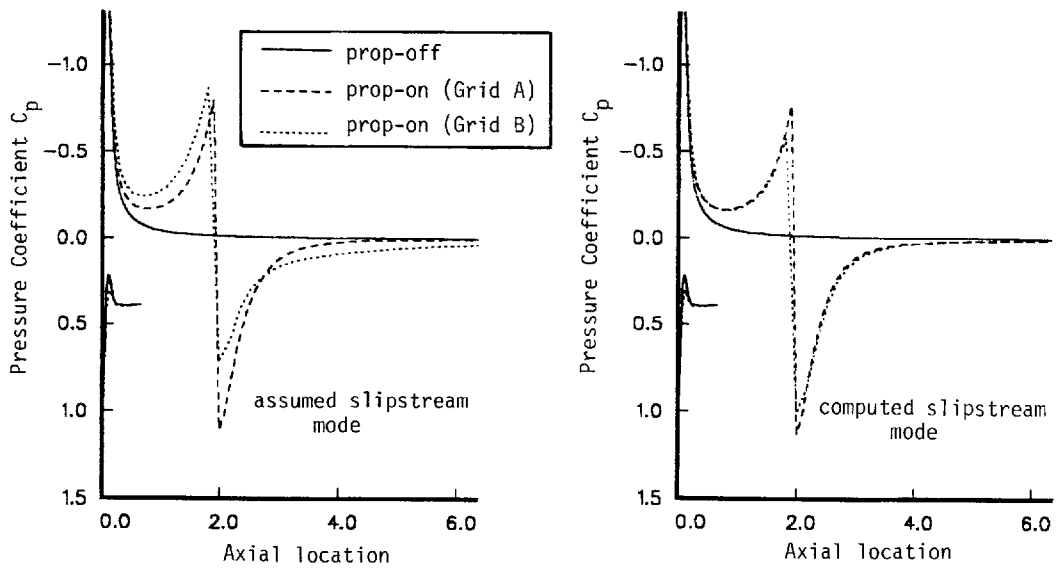

Figure 9. Effect of grid on nacelle surface pressure distribution

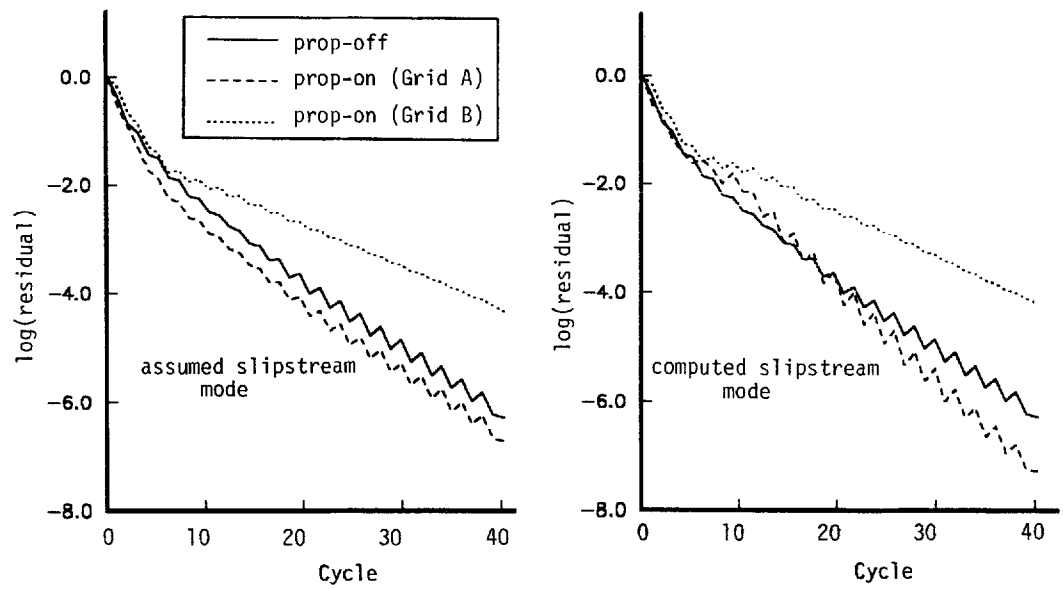

Figure 10. Effect of grid on convergence history

Figure 10 shows the comparisons of the convergence history for the calculations presented in Figure 9. Two observations can be drawn from this figure. First, in both the assumed and computed slipstream mode calculations, the convergence rate of the grid A prop-on solution is roughly the same as that of the original prop-off solution while the convergence rate of the grid B prop-on solution deteriorates relative to that of the original prop-off solution. This indicates

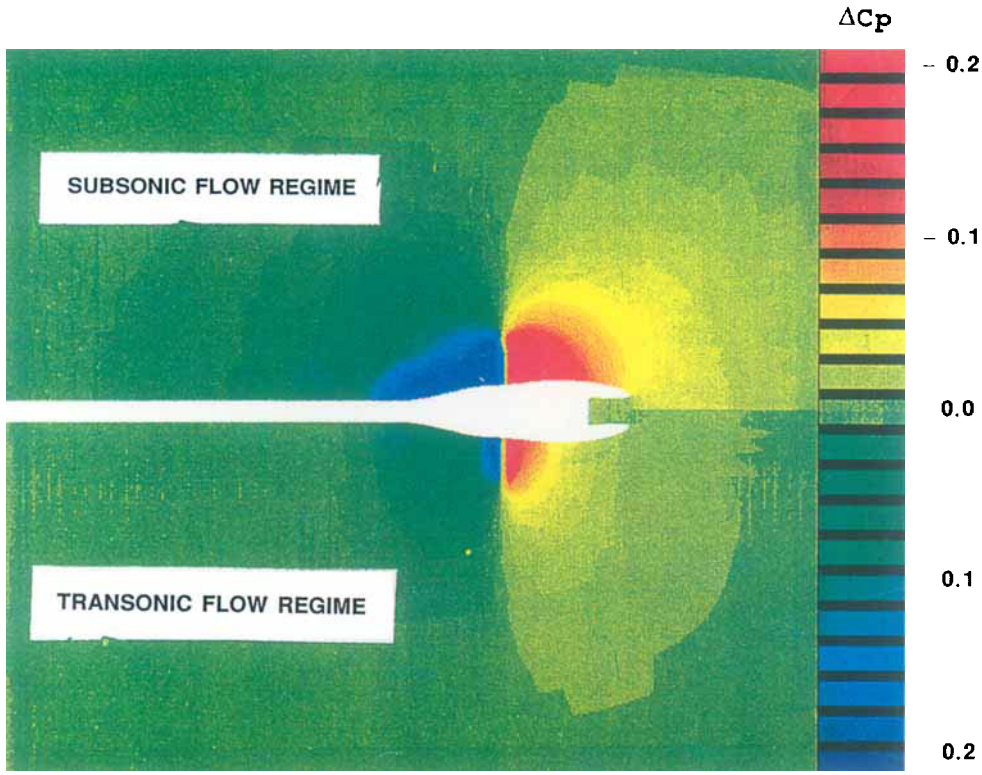

Plate 1. Contour of pressure coefficient increment about nacelle C

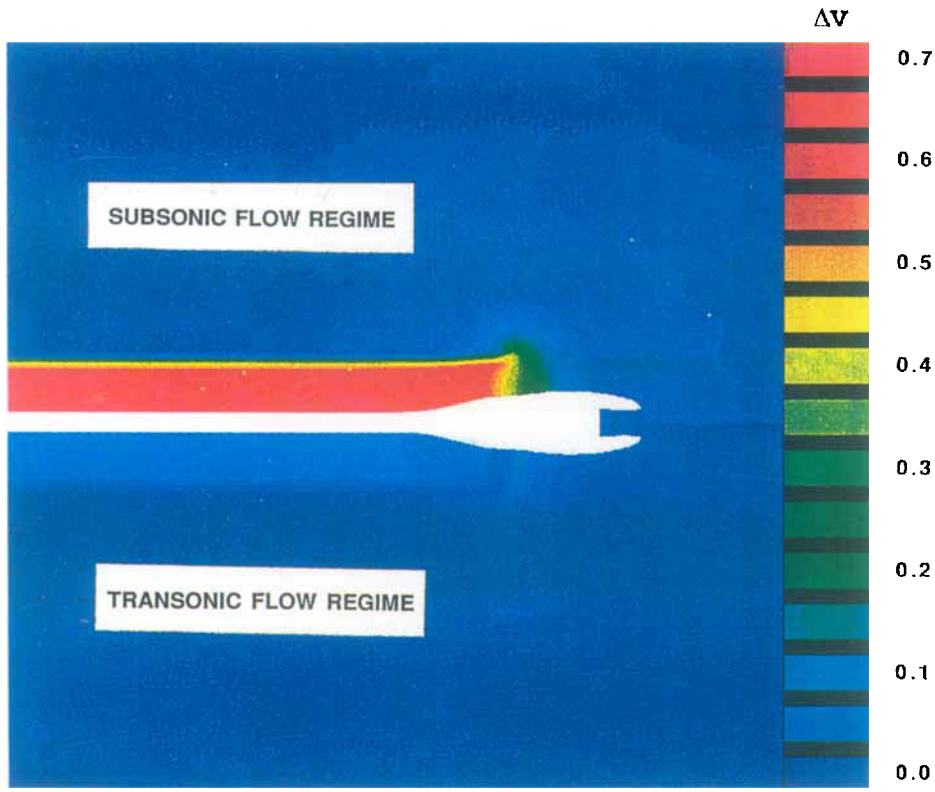

Plate 2. Contour of velocity increment about nacelle C

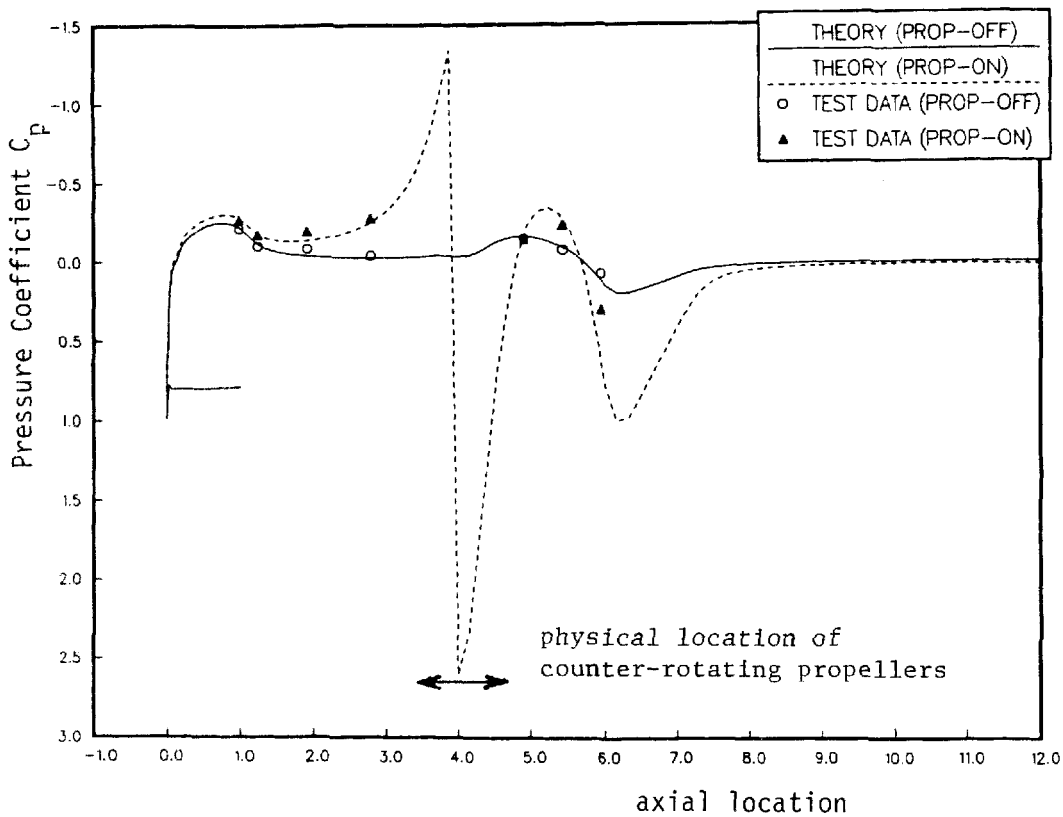

Figure 11. Comparisons of surface pressure distributions between theoretical predictions and experimental data

that in the general three-dimensional case, such as angle of attack and/or complex configurations, the situation corresponding to grid B is likely to be encountered and it is expected that more iterations are required to obtain converged solutions comparable to the original prop-off solutions. Second, for a given grid distribution, Figure 10 indicates that the convergence rate between the assumed and computed slipstream modes are virtually the same. This figure indicates that the present method of computing vortex sheets is efficient.

Finally, Figure 11 illustrates an excellent agreement in the surface pressure distribution between computational results and experimental data in the subsonic-flow regime at a relatively high thrust loading coefficient. Note that the comparison is not only good in front of the propeller but also behind the propeller, even though the flowfield is expected to be highly rotational in the region within the propeller slipstream behind the propeller.

6. CONCLUSIONS

This paper presents a numerical technique for handling vortex sheets in full-potential methods. The idea is to remove singularities in the flowfield at the vortex sheet using the 'smoothing' technique: all discontinuities are expressed in terms of the step function. In addition, the location and strength of the vortex sheets are determined by satisfying the flow-tangency boundary condition and the vorticity transport equation.

In order to facilitate the task of describing the technique, the example of computing propeller slipstream, which arises from the modelling of a counter-rotating propeller by an actuator disk with free-vortex blading, is presented. In this case, the flowfield consists of two potential-flow regions of different stagnation conditions, separated by a bound-vortex sheet at the actuator disk and a free-vortex sheet on the propeller slipstream. Along the propeller slipstream, both the kinematic condition (flow-tangency boundary condition) and the dynamic condition (vorticity transport equation) are satisfied. This method has been successfully embedded into a finite-volume full-potential code for the simulation of propeller effects about isolated nacelles in axisymmetric flows. The same method has also been implemented into an aft-fuselage/pylon/nacelle computer code to study power effects in the presence of a counter-rotating propfan of the pusher type.[30]

The following conclusions can be extracted from the numerical experiments:

1. The method preserves the inviscid nature of discontinuities across vortex sheets because the scheme does not contain numerical dissipation.
2. The method gives solutions which are insensitive to mesh distribution.
3. The method is not penalized in the convergence rate when the computed slipstream mode is employed.

The examples used in this paper (for axisymmetric flows) and in Reference 30 (for three-dimensional flows) involve vortex sheets that do not have excessive distortions. In cases where the vortex sheets have large deformations, such as the rolling up of the trailing-vortex sheet near the wing tip, the theory presented here is still valid, but a more elaborate numerical technique is needed to track the position of the vortex sheet. The use of Clebsch variables to track highly distorted material lines in inviscid shear layers has been demonstrated.[34] In this method, a uniformly second-order-accurate, non-oscillatory convection scheme is used to solve the convection equations representing the rotational component of the flowfield.

ACKNOWLEDGEMENTS

The work reported in this paper was conducted at the Douglas Aircraft Company under the sponsorship of the Independent Research and Development Program of the McDonnell Douglas Corporation. The author would like to acknowledge Mr. N. D. Halsey and Dr. A. Shmilovich for their assistance in the grid generation method and the unpowered version of the potential-flow solver, respectively.

REFERENCES

1. A. Jameson and D. A. Caughey, 'A finite-volume method for transonic potential flow calculations', *Proc. AIAA 3rd Computational Fluid Dynamics Conference*, Albuquerque, NM, June 1977, pp. 35–54.
2. D. A. Caughey and A. Jameson, 'Numerical calculation of transonic potential flow about wing–body combinations', *AIAA J.*, **17**, 175–181 (1979).
3. E. M. Murman and J. D. Cole, 'Calculation of plane steady transonic flows', *AIAA J.*, **9**, 114–121 (1971).
4. L. T. Chen, J. C. Vassberg and C. C. Peavey, 'A transonic wing–body flowfield calculation with an improved grid topology', *AIAA J.*, **23**, 1877–1884 (1985).
5. A. Jameson, 'Acceleration of transonic potential flow calculations on arbitrary meshes by the multiple grid method', *AIAA Paper 79-1458*, July 1979.
6. A. Shmilovich and D. A. Caughey, 'Application of the multi-grid method to calculations of transonic potential flow about wing–fuselage combinations', *NASA SP-2202*, October 1981, pp. 101–130.
7. M. Hafez and D. Lovell, 'Entropy and vorticity corrections for transonic flows', *AIAA Paper 83-1926*, 1983.
8. G. H. Klopfer and D. Nixon, 'Non-isentropic potential formulation for transonic flows', *AIAA Paper 83-0375*, 1983.
9. T. Q. Dang and L. T. Chen, 'An Euler correction method for two- and three-dimensional transonic flows', *AIAA J.*, **27**, 1377–1386 (1989).

10. A. Jameson, W. Schmidt and E. Turkel, 'Numerical solutions of the Euler equations by finite volume methods using Runge–Kutta time-stepping schemes', *AIAA Paper 81-1259*, June 1981.
11. A. Jameson and T. J. Baker, 'Multigrid solution of the Euler equations for aircraft configurations', *AIAA Paper 84-93*, 1984.
12. T. Q. Dang, 'Simulations of propeller/airframe interference effects using an Euler correction method', *J. Aircraft*, **26**, 994–1001 (1989).
13. B. Zaretsky, T. Q. Dang, A. Shmilovich and N. D. Halsey, 'Calculation of propeller effects on axisymmetric nacelles with and without inlets', *Report No. MDC J4920*, Douglas Aircraft Company, October 1986.
14. J. Steinhoff and K. Ramachandran, 'Free-wake analysis of compressible rotor flows', *AIAA J.*, **28**, 426–431 (1990).
15. M. J. Lighthill, *An Introduction to Fourier Analysis and Generalized Functions*, Cambridge University Press, Cambridge, 1969.
16. J. E. McCune and T. Q. Dang, 'Periodic internal flows', in P. M. Sockel and K. N. Ghia (eds), *Proc. ASME Conf. on Computations of Internal Flows: Methods and Applications*, pp. 123–128, 1984.
17. T. Q. Dang and J. E. McCune, 'A 3D blade design method in rotational flow', in G. S. Dulikravich (ed.), *Proc. Int. Conf. on Inverse Design Concepts in Engineering Sciences*, University of Texas, Austin, 1984, pp. 397–417.
18. T. Q. Dang, 'A three-dimensional blade method to control secondary flow', *Ph.D. Thesis*, Department of Aero/Astro, Massachusetts Institute of Technology, Cambridge, 1985.
19. D. L. Whitfield and A. Jameson, 'Three-dimensional Euler equation simulation of propeller–wing interaction in transonic flow', *AIAA Paper 83-0235*, 1983.
20. N. J. Yu, S. S. Samart and P. E. Rubbert, 'Flow prediction for propfan configurations using Euler equations', *AIAA Paper 84-1645*.
21. D. P. Golden, T. J. Barber and W. C. Chin, 'An axisymmetric nacelle and turboprop inlet analysis including power simulation', *J. Aircraft*, **20**, 536–542 (1983).
22. W. R. Hawthorne, On the theory of shear flow', *Report No. 88*, MIT Gas Turbine Laboratory, 1966.
23. J. E. McCune and W. R. Hawthorne, 'The effects of trailing vorticity on the flow through highly-loaded cascades', *J. Fluid Mech.*, **74**, 721–740 (1976).
24. W. R. Hawthorne, N. A. Mitchell, J. E. McCune and C. S. Tan, 'Nonaxisymmetric flow through an annular actuator disk: inlet distortion problem', *ASME J. Eng. Power*, **100**, 604–617 (1978).
25. C. S. Tan, 'Vorticity modeling of blade wakes behind isolated annular blade rows: induced disturbances in swirling flows', *ASME J. Eng. Power*, **103**, 279–287 (1981).
26. W. R. Hawthorne, C. Wang, C. S. Tan and J. E. McCune, 'Theory of blade design for large deflections: Part 1—2D cascade, Part 2 Annular cascade', *J. Eng. Gas Turbines Power*, **106**, 346–365 (1984).
27. W. S. S. Ghaly, 'A design method for turbomachinery blading in three-dimensional flow', *Int. j. numer methods fluids*, **10**, 179–197 (1990).
28. M. J. Lighthill, 'Drift', *J. Fluid Mech.*, **1**, 31–53 (1956).
29. G. R. Baker, 'The 'cloud in cell' technique applied to the roll up of vortex sheets', *J. Comput. Phys.*, **31**, 76–95 (1979).
30. T. Q. Dang, 'Calculations of propeller/airframe interference effects using the potential/multienergy flow method', *AIAA J.*, **28**, 771–777 (1990).
31. A. Shmilovich and D. A. Caughey, 'On transonic flow computations about airfoils, axisymmetric projectiles and nacelles in free air and in wind tunnels', *Report No. MDC J3852*, Douglas Aircraft Company, October 1985.
32. N. D. Halsey, 'Use of conformal mapping in grid generation for complex three-dimensional configurations', *AIAA J.*, **15**, 1286–1291 (1987).
33. T. Q. Dang, 'Accurate treatment of vortex sheets for the transonic potential equation with application to propeller slipstream', *Report No. MDC K1342*, Douglas Aircraft Company, June 1988.
34. J. W. Yokota, 'Vorticity dynamics of shear layers', *AIAA Paper 92-0420*, 1992.